Accelerating Materials-Space Exploration by Mapping Materials Properties via Artificial Intelligence: The Case of the Lattice Thermal Conductivity

Thomas A. R. Purcell,[1,*] Matthias Scheffler,[1,2] Luca M. Ghiringhelli,[1,2,†] and Christian Carbogno[1,‡]

[1] *The NOMAD Laboratory at Fritz-Haber-Institut der Max-Planck-Gesellschaft, Faradayweg 4–6, D-14195 Berlin, Germany*
[2] *FAIRmat at Humboldt Universität zu Berlin, Berlin, Germany.*

(Dated: April 28, 2022)

Accurate artificial-intelligence models are key to accelerate the discovery of new functional materials with optimal properties for various applications. Examples include superconductivity, catalysis, and thermoelectricity. Advancements in this field are often hindered by the scarcity and quality of available data and the significant effort required to acquire new data. For such applications, reliable surrogate models that help guide materials space exploration using easily accessible materials properties are urgently needed. Here, we present a general, data-driven framework that provides quantitative predictions as well as qualitative rules for steering data creation for all datasets via a combination of symbolic regression and sensitivity analysis. We demonstrate the power of the framework by generating an accurate analytic model for the lattice thermal conductivity using only 75 experimentally measured values. By extracting the most influential material properties from this model, we are then able to hierarchically screen 732 materials and find 80 ultra-insulating materials.

I. INTRODUCTION

Artificial-intelligence (AI) techniques have the potential to significantly accelerate the search for novel, functional materials, especially for applications where different physical mechanisms compete with each other nonlinearly, e.g., quantum materials [1], and where the cost of characterizing the materials makes a large-scale search intractable, e.g., thermoelectrics [2]. Due to this inherent complexity, only limited amounts of data are currently available for such applications, which in turn severely limits the applicability and reliability of AI techniques [3]. Using thermal transport as an example, we here propose a route to overcome this hurdle by presenting an AI framework that is applicable to scarce datasets and that provides heuristics able to steer further data creation into materials-space regions of interest.

Heat transport, as measured by the temperature-dependent thermal conductivity, κ_{L}, is an ubiquitous property of materials and plays a vital role for numerous scientific and industrial applications including energy conversion [4], catalysis [5], thermal management [6], and combustion [7]. Finding new crystalline materials with either an exceptionally low or high thermal conductivity is a prerequisite for improving these and other technologies or making them commercially viable at all. Accordingly, finding new thermally insulating materials and understanding where in materials space to search for such compounds is an important open challenge in this field. From a theory perspective, thermal transport depends on a complex interplay of different mechanisms, especially in thermal insulators, for which strongly anharmonic, higher-order effects can be at play [8]. Despite significant progress in the computational assessment of κ_{L} in solids [9, 10], these *ab initio* approaches are too costly for a large-scale exploration of material space. For this reason, computational *high-throughput* approaches have so far covered only a small subset of materials [11–13]. Experimentally, an even smaller number of materials have had their thermal conductivities measured, and less than 150 thermal insulators identified [14, 15].

Recently, increased research efforts have been devoted to leveraging AI frameworks to extend our knowledge in this field. In particular, various regression techniques have been proven to successfully interpolate between the existing data and approximate κ_{L} using only simpler properties [11, 14, 16, 17]; however, using these techniques to extrapolate into new areas of materials space is a known challenge. Physically motivated, semi-empirical models, e.g. the Slack model [18], perform slightly better in this regard because they encapsulate information about the actuating mechanism. Recent efforts have used AI to extend the capabilities of these models [2, 16, 19, 20] to increase their accuracy in estimating κ_{L}. However, applicability of such models is still limited by the physical assumptions entering the original expressions. [2, 19]. A general model that removes these assumptions and achieves the quantitative accuracy of AI approaches, while retaining the qualitative interpretability of analytical models, is, however still lacking.

In this work, we tackle this challenge by using a symbolic regression technique to quantitatively learn κ_{L}, using easily calculated materials properties. As demonstrated using a global sensitivity analysis method, this enables us to distill out the key material properties that are most important for modelling κ_{L} and find the conditions necessary for obtaining an ultra-low thermal conductivity. From these heuristics we can then establish qualitative design principles that lend themselves to general application across material space and use them to find 80 materials with an ultra-low κ_{L}.

* purcell@fhi-berlin.mpg.de
† ghiringhelli@fhi-berlin.mpg.de
‡ carbogno@fhi-berlin.mpg.de

II. RESULTS

A. Symbolic Regression Models for Thermal Conductivity

For this study, we use the sure-independence screening and sparsifying operator (SISSO) method as implemented in the SISSO++ code [21]. This method has been used to successfully describe multiple applications including the stability of materials [22], catalysis [23], and glass transition temperatures [24]. To find the best low-dimensional models for a specific target property, in our case the room temperature, lattice thermal conductivity, $\kappa_L\,(300\text{K})$, SISSO first builds an exhaustive set of analytical, non-linear functions, i.e. trillions of candidate descriptors, from a set of mathematical operators and primary features, the set of user-provided properties that will be used to model the target property. For this application the primary features are both the structural and dynamical features for seventy-five materials with experimentally measured $\kappa_L\,(300\text{K})$ (see Section VI C for more details) [17, 25–42].

In practice, we model the $\log\left(\kappa_L\,(300\text{K})\right)$ instead of $\kappa_L\,(300\text{K})$ itself to better handle the wide range of possible thermal conductivities. The correlation plot in Figure 1(a) illustrates the performance of the identified SISSO model when the entire dataset is used (see Section VI A for more details). The resulting expression is characterized by f_0 and f_1

$$\begin{aligned}\log\left(\kappa^{\text{SISSO}}\,(300\text{K})\right) &= c_0 + a_0 f_0 + a_1 f_1\\ f_0 &= \frac{\left(m_{\text{avg}} + 200.3\,\text{Da}\right)^2}{\sqrt{\mu}\left(V_{\text{m}} + 218.9\,\text{Å}^3\right)^3\,\Theta_{\text{D},\infty}\sigma^{\text{A}}}\\ f_1 &= \sigma^{\text{A}}\frac{V_{\text{m}}\rho}{m_{\text{avg}}} + e^{\frac{-\omega_{\Gamma,\text{max}}}{27.11\,\text{THz}}} + e^{\sigma^{\text{A}}}\end{aligned} \tag{1}$$

where $c_0 = 6.327$, $a_0 = -8.219\times10^4$, and $a_1 = -1.704$ are constants found by least-square regression and all variables are defined in Table II. We find that this model has a training root-mean squared error (RMSE) of 0.14, with an R^2 of 0.98 for $\log\left(\kappa^{\text{SISSO}}\,(300\text{K})\right)$. To better understand how these error terms translate to $\kappa_L\,(300\text{K})$, we also use the average factor difference (AFD)

$$\text{AFD} = 10^x \tag{2a}$$

$$x = \frac{1}{n}\sum_i^n \left|\log\left(\kappa_{\text{L}}\right) - \log\left(\kappa_{\text{L}}^{\text{pred}}\right)\right|, \tag{2b}$$

where n is the number of training samples. Here, we find an AFD of 1.30 that is on par if not superior to the models previously found by other methods (e.g. 1.38 for a Gaussian Process Regression model [17] and 1.48 for a semi-empirical Debye-Callaway Model [2]). However, differences in the training sets and cross-validation scheme prevent a fair comparison of these studies.

To get a better estimate on the prediction error, we use a nested cross-validation scheme further defined in Section VI D. Overall the prediction error is slightly higher than the training error with an RMSE of 0.22 ± 0.02, R^2 of 0.91 ± 0.01, and AFD of 1.45 ± 0.03. As shown in Fig. 1(b), these errors are comparable to those of a kernel ridge regression (KRR) model trained on the same data. This substantiates that our symbolic regression approach performs as well as interpolative methods and outperform the Slack model. Interestingly, offering the features of the Slack model to SISSO does not improve the model, and even some primary features often thought to be decisive, e.g., the Grüneisen parameter, γ. are not even selected by SISSO (see Supplementary Note 3).

In contrast to the interpolative models, the SISSO models not only yield reliable quantitative predictions, but also allows for a qualitative inspection of the underlying mechanisms. To get a better understanding of how the thermal conductivity changes across materials space we map the model in Figure 1c. From this map we can see that the thermal conductivity of a material is mostly controlled by f_1 with f_0 providing only a minor correction. While these observed trends are already helpful, the complex non-linearities in both f_0 and f_1 impedes the generation of qualitative design rules. Furthermore, some primary features such as V_{m} and σ^{A} enter both f_0 and f_1, with contrasting trends, e.g., σ^{A} lowers f_0 but increases f_1. To accelerate the exploration of materials space, one must first be able to disentangle the contradicting contributions of the involved primary features.

B. Extracting Physical Understanding by identifying the Most Physically Relevant Features via Sensitivity Analysis

The difficulties in interpreting the "plain" SISSO descriptors described above can be overcome by performing a sensitivity analysis to identify the most relevant primary features that build f_0 and f_1. For this purpose, we employ the Sobol indices, i.e., the first order sensitivity index S_i and the total sensitivity index S_i^T, using an algorithm that includes correlative effects first described by Kucherenko *et al.* [43], and later implemented in UQLab [44, 45]. The main advantage of this approach is its ability to include correlative effects between the inputs, which if ignored can largely bias or even falsify the sensitivity analysis results [46]. Qualitatively, the first order sensitivity index, S_i, quantifies how much the variance of $\log\left(\kappa_L\,(300\text{K})\right)$ correlates with the variance of a primary feature, $\hat{x}_i$, and the total sensitivity index, S_i^T quantifies how much the variance of $\log\left(\kappa_L\,(300\text{K})\right)$ correlates with $\hat{x}_i$ including all interactions between $\hat{x}_i$ and the other primary features. For example, Sobol indices of 0.0 indicate that $\log\left(\kappa_L\,(300\text{K})\right)$ is fully independent of $\hat{x}_i$, whereas a value of 1.0 indicates that $\log\left(\kappa_L\,(300\text{K})\right)$ can be completely represented by changes in $\hat{x}_i$ [45]. Moreover, $S_i^T < S_i$ implies that correlative effects are

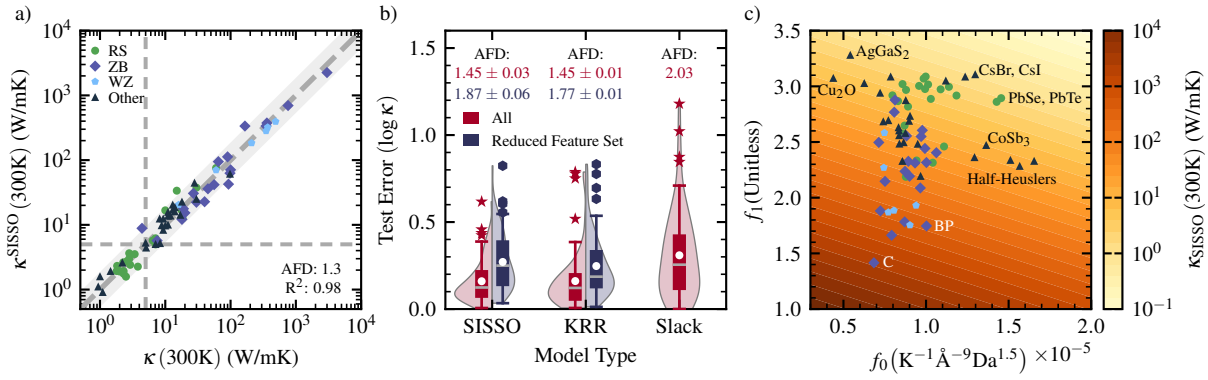

FIG. 1. a) Comparison of the predicted κ^{SISSO} (300K) against the measured κ_L (300K) for the model trained against all data. The gray shaded region corresponds to 95% confidence interval. b) Violin plots of the mean prediction error of all samples for both the SISSO and KRR models using all features (red, left) and a reduced set including only the features bolded in Table I (blue, right) and the Slack model. Gray lines are the median, white circles are the mean of the distributions, the boxes represent the quartiles, and the whiskers are the minimum and 95% absolute error. For all calculations the rung and dimension determined by cross-validation on each training set. The red stars and blue hexagons are the outliers for the box plots. c) A map of the two-dimensional SISSO model, where the features on the $x-$ and $y-$axes correspond to the two features selected by SISSO. The labeled points represent the convex-hull of the scatter plot and related points.

significant, with an $S_i^T = 0$ indicating that a primary feature is perfectly correlated to the other inputs [45].

TABLE I. Sensitivity Analysis results for the selected model

	ρ	$\boldsymbol{\Theta_{\mathrm{D},\infty}}$	$\boldsymbol{V_{\mathrm{m}}}$	m_{avg}	$\boldsymbol{\sigma^{\mathrm{A}}}$	$\omega_{\Gamma,\mathrm{max}}$	μ
S_i	0.05	**0.67**	**0.54**	0.37	**0.65**	0.63	0.14
S_i^T	0.03	**0.01**	**0.02**	0.01	**0.04**	0.01	0.01

Table I summarizes the Sobol indices for κ^{SISSO} (300K). The results for S_i show that σ^{A}, V_{m}, $\Theta_{\mathrm{D},\infty}$, and $\omega_{\Gamma,\mathrm{max}}$ predominately control the variance of κ^{SISSO} (300K). However, the low values of S_i^T also imply that there are significant correlative effects in place between these inputs, and no single feature can be singled out as primarily responsible for changes in κ^{SISSO} (300K). For instance, because $\omega_{\Gamma,\mathrm{max}}$ and $\Theta_{\mathrm{D},\infty}$ are strong correlated to each other, only one of them needs to be considered (see the Supplementary Figure 2). The importance of these features is further substantiated in Figure 1b, where we compare the performance of the models calculated using the full dataset and one that only includes the three features in bold in Table I. For both the SISSO and KRR models, we see only a slight deterioration in performance with a predictive AFD of 1.87 and 1.77 for the SISSO and KRR models, respectively, compared to 1.45 for the full data models. This result highlights that the trends and the underlying mechanisms describing the dependence of κ_L (300K) in materials space are fully captured by those features alone.

Even more importantly, our model captures the interplay between these features across materials, as demonstrated in the maps in Figure 2. These maps showcase the strong correlation between κ^{SISSO} (300K) and σ^{A}, V_{m}, and $\Theta_{\mathrm{D},\infty}$, and that materials with high anharmonicity, low-energy vibrational modes, and a large molar volume will be good thermal insulators. Figure 2 shows the expected value of κ^{SISSO} (300K), $E_{\hat{\mathcal{X}}}\left(\kappa^{\text{SISSO}}\left(300\text{K}\right)\middle|\,\hat{\mathcal{X}}\right)$, for different sets of input features, $\hat{\mathcal{X}}$, shown on the axes of each plot. We then overlay the maps with the actual values of each input for all materials in the training set to evaluate the trends across different groups of materials. Figure 2c confirms that σ^{A} is already a good indicator for finding new thermal insulators, with most of the materials having κ_L (300K) within one standard deviation of the expected value. For the more harmonic materials with $\sigma^{\mathrm{A}} < 0.2$, the vanishing degree of anharmonicity is, alone, not always sufficient for quantitative predictions. In this limit, a combination of σ^{A} and V_{m} can produce correct predictions for the otherwise underestimated white triangles with a $\sigma^{\mathrm{A}} < 0.2$, as seen in Figure 2a. In order to fully describe those low thermal conductivity of the remaining highlighted materials materials both $\Theta_{\mathrm{D},\infty}$ and V_{m} are needed as can be seen in Figure 2b,d and e. Generally, this reflects that the **three** properties σ^{A}, $\Theta_{\mathrm{D},\infty}$, and V_{m} are the target properties to optimize to obtain ultra-low thermal conductivities.

These results can also be rationalized within our current understanding of thermal transport and showcases which physical mechanisms determine κ_{L} in material space. Qualitatively, it is well known that good thermal conductors typically exhibit a high degree of symmetry with a smaller number of atoms, e.g. diamond and silicon, whereas thermal insulators, e.g., glass-like materials, are often characterized by an absence of crystal symmetries and larger primitive cells. In our case, this trend is quantitatively captured via V_{m}, which reflects that larger unit cells have smaller thermal conductivities.

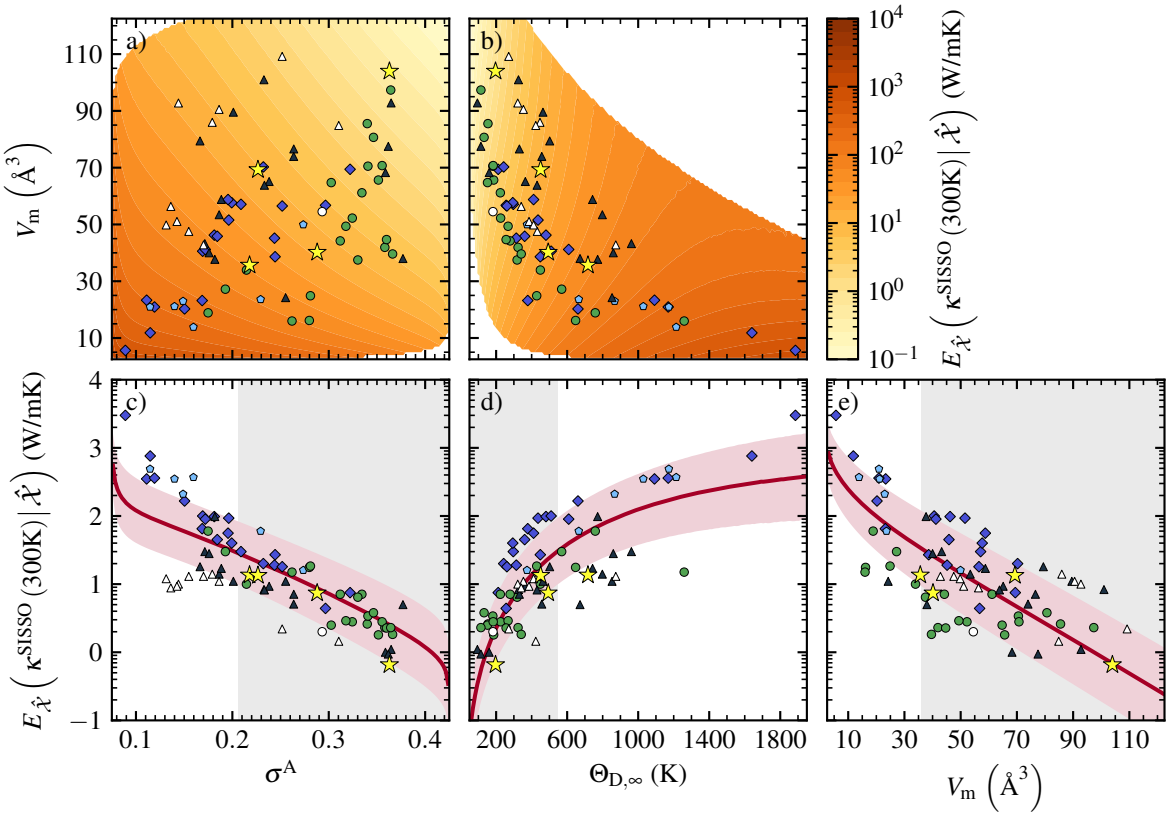

FIG. 2. The expected value of $\kappa^{\mathrm{SISSO}}(300\mathrm{K})$, $E_{\hat{\mathcal{X}}}\left(\kappa^{\mathrm{SISSO}}(300\mathrm{K})|\hat{\mathcal{X}}\right)$, where $\hat{\mathcal{X}}$ is a) $\{\sigma^A, V_m\}$, b) $\{\Theta_{D,\infty}, V_m\}$, c) $\{\sigma^A\}$, d) $\{\Theta_{D,\infty}\}$, and e) $\{V_m\}$. $E_{\hat{\mathcal{X}}}\left(\kappa^{\mathrm{SISSO}}(300\mathrm{K})|\hat{\mathcal{X}}\right)$ is calculated by sampling over the multivariate distributions used for the sensitivity analysis, and binning the input data until there are at least 10 000 samples in each bin. The red line in c-e corresponds to $E_{\hat{\mathcal{X}}}\left(\kappa^{\mathrm{SISSO}}(300\mathrm{K})|\hat{\mathcal{X}}\right)$ and the pink shaded region is one standard deviation on either side of the line. The gray shaded regions represent where a thermal conductivity of 10 W/mK or lower is within one standard deviation of the expected value. On all maps all materials in the training set are displayed. The green circles correspond to rock-salts, the blue diamonds are zincblende, the light blue pentagons are wurtzites, and black triangles are all other materials. All points with a κ_L (300K) less than one standard deviation below the expected value based on σ^A are highlighted in white. The points in c-e correspond to the actual values of κ_L (300K) for each material. Additionally we include four new materials outside of the training set (yellow stars) whose thermal conductivities we calculate using *ab initio* molecular dynamics.

Furthermore, it is well known that phonon group velocities determine how fast energy is transported through the crystal in a harmonic picture [47], and that it is limited by scattering events arising due to anharmonicity. In our model, these processes are captured by $\Theta_{D,\infty}$, which describes degree of dispersion in the phonon band structure, and the anharmonicity measure, σ^A respectively. In this context, it is important to note that, in spite of the fact that these qualitative mechanisms were long known, there had hitherto been no agreement which material property would quantitatively capture these mechanisms best across material space. For instance, both the γ, the lattice thermal expansion coefficient, and now σ^A, have been used to describe the anharmonicity of a material. However, when both γ and σ^A are included as primary features, only σ^A is chosen (see Supplementary Note 3 for more details). This result indicates that the σ^A measure is the more sensitive choice for modeling the strength of anharmonic effects. While γ also depends on anharmonic effects, they are also influenced by the bulk modulus, the density, and the specific heat.

C. Discovering Improved and Novel Thermal Insulators

Using the information gained from the sensitivity analysis and statistical maps of the model, we are now able to design a hierarchical and efficient high-throughput screening protocol split into three stages: structure optimization, harmonic model generation, and anharmonicity quantification. We demonstrate this procedure by identifying possible thermal insulators within a set of 732 materials, within those compounds available in the materials project [48] that feature the same crystallographic prototypes [49, 50] as the ones used for training. Once

the geometry is optimized we remove all materials with $V_m < 35.5$ Å(60 materials) and all (almost) metallic materials (bandgap < 0.2 eV), and are left with 302 candidate compounds. We then generate the converged harmonic model for the remaining materials and screen out all materials with $\Theta_{D,\infty} > 547$ K or an unreliable harmonic model, e.g. materials with imaginary harmonic modes, leaving 148 candidates. Finally we evaluate the anharmonicity, σ^A, for the remaining materials (see Section VI C) and exclude all materials with $\sigma^A < 0.206$, and obtain 110 candidate thermal insulators. To avoid unnecessary calculations, we first estimate σ^A via σ^A_{OS} and then refine it via aiMD when $\sigma^A_{OS} > 0.4$ [8]. For these candidate materials, we evaluate κ^{SISSO} (300K) using Eq. 1. Of the 110 materials that passed all checks, 96 are predicted to have have a κ^{SISSO} (300K) below 10 W/mK l, illustrating the success of this method.

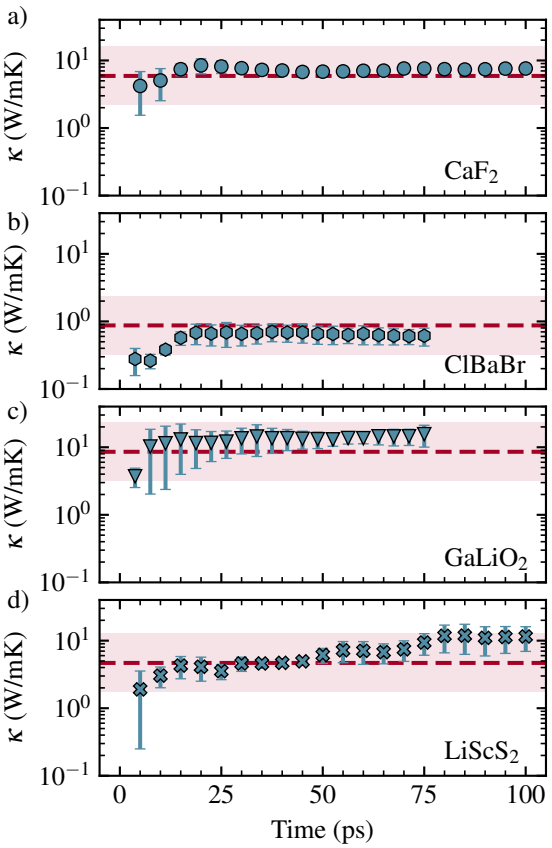

FIG. 3. The convergence of the calculated thermal conductivity of a) CaF_2, b) BrBaCl, c) $GaLiO_2$ d) $LiScS_2$. All aiGK calculations were done using the average of three 75 ps (ClBaBr and $GaLiO_2$) or 100 ps (CaF_2 and $LiScS_2$) molecular dynamics trajectories. The dashed lines are the values of the thermal conductivities predicted by Equation 1 and the shaded region is the 95% confidence interval of the prediction based on the RMSE obtained in Figure 1b.

To confirm that our approach is not just consistent with the SISSO model, but also produces physically meaningful predictions, we validate the estimated thermal conductivity of four materials using the *ab initio* Green-Kubo method (aiGK) [10]. For details of how we calculate κ_L see the methodology in Section VI G. For this purpose, we chose BrBaCl, $LiScS_2$, CaF_2, and $GaLiO_2$, since these materials represent a broad region of the relevant feature space that also test the boundary regions of the heuristics found by the sensitivity analysis and mapping, as demonstrated by the yellow stars in Figure 2. Figure 3 shows the convergence of the thermal conductivity of the selected materials, as calculated from three aiMD trajectories. All of the calculated thermal conductivities fall within the 95% confidence interval of the model, with the predictions for both CaF_2 and ClBaBr being particularly accurate. The better performance of the model for these materials is expected, as they are more similar to the training data than the hexagonal Caswellsilverite like materials. Overall these results demonstrate the predictive power of the new model.

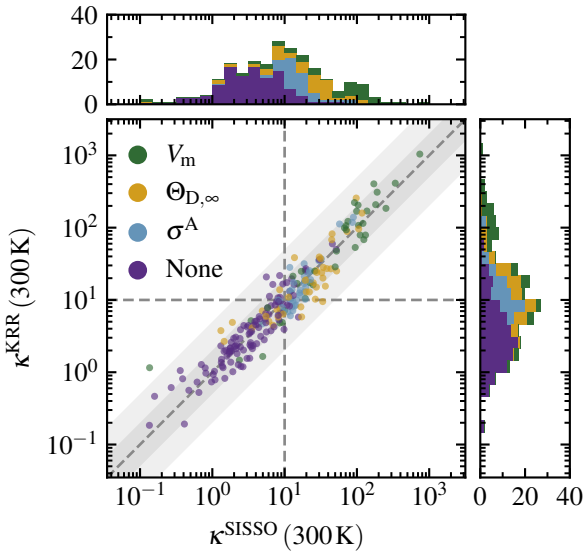

FIG. 4. A scatter plot of of the prediction of both the SISSO and KRR generated models for an additional 227 materials from the same classes as the training set. σ^A is estimated via σ^A_{OS} for all materials with a $\sigma^A_{OS} \leq 0.4$ in this screening. The dataset is split up into four subsets based on if the V_m test failed (top, green), $\Theta_{D,\infty}$ test failed (second from top, yellow), σ^A test failed (third from top, blue), or none of the tests failed (bottom, purple). The outlets correspond to the histogram of all predictions using the same break down. The darker shaded region represents where both predictions are within a factor of 2 of each other and the lighter shaded region where both predictions are within a factor of 5 of each other.

Eventually, let us emphasize that the proposed strategy is not limited to the discovery of thermal insulators, but can be equally used to find, e.g., good thermal conductors. This is demonstrated in Figure 4, in which we predict the thermal conductivity of all non-metallic and stable materials using the SISSO and KRR models. Generally, both the SISSO and KRR models agree with each

other with only 28 of the 227 materials having a disagreement larger than a factor of two and one ($LiHF_2$) with a disagreement larger than a factor of 5, further illustrating the reliability of these predictions. We expect that the large deviation for $LiHF_2$ is a result of the large σ^{A} value for that material (0.54), which is significantly larger than the maximum the training data. We can see from the outset histograms of both models that the hierarchical procedure successfully finds the good thermal insulators, with only 26 of the 122 materials with a $\kappa_L\,(300\mathrm{K}) \leq 10$ W/mK and 10 of the 80 materials with a $\kappa_L\,(300\mathrm{K}) \leq 5$ W/mK not passing all tests. Of these eight only the thermal insulating behavior of $CuLiF_2$ and Sr_2HN can not be described by the values of the other two tests that passed. Conversely, materials that do not pass the test show high conductivities. When one of the tests fail the average estimated value of $\log\left(\kappa_L\,(300\mathrm{K})\right)$ increases 1.38 ± 0.490 (24.0 W/mK), with a range of 0.95 W/mK to 741.3 W/mK. In particular, screening the materials by their molar volumes alone is a good marker for finding strong thermal conductors as all of the 15 materials with $\kappa_L\,(300\mathrm{K}) \geq 100$ W/mK have a $V_{\mathrm{m}} \leq 45$ Å^3.

III. DISCUSSION

We have developed an AI framework to facilitate and accelerate material space exploration, and demonstrate its capabilities for the urgent problem of finding new thermally insulating materials. By combining symbolic regression and sensitivity analysis, we are able to obtain accurate predictions for a given property using relatively easy to calculate materials properties, while retaining strong physical interpretability. Most importantly, this analysis enables us to create hierarchical high-throughput frameworks, which we used to screen over a set of more than 700 materials and find a group of $\sim$ 100 possible thermal insulators. Notably, almost all of the good thermal conductors in the set of candidate materials are discarded within the first iteration of the screening, in which we only discriminate by molar volume, i.e., with an absolutely negligible computational cost compared to full calculations of κ_{L}. Accordingly, we expect this approach to be extremely useful in a wide range of materials problems beyond thermal transport, especially whenever (i) few reliable data are available, (ii) additional data are hard to produce, and/or (iii) multiple physical mechanisms compete non-trivially, limiting the reliability of simplified models.

Although the proposed approach is already extremely useful for small dataset sizes, it is obviously getting more reliable when applied to larger ones. Here, the identified heuristics can substantially help steer data creation towards more interesting parts of material space. Along these lines, it is possible to iteratively refine both the SISSO model and the rules from the sensitivity analysis during material space exploration while the dataset grows. Furthermore, one can also apply the proposed procedure to the most influential primary features in a recursive fashion, learning new expressions for the computationally expensive features, e.g. σ^{A}, using simpler properties. In turn, this will further accelerate material discovery, but also allow for gaining further physical insights. Most importantly, this method is not limited to just the thermal conductivity of a material, and can be applied to any materials property. Further extending this framework to include information about where the underlying electronic structure calculations are expected to fail, also provides a means of accelerating materials discovery more generally [51].

IV. ACKNOWLEDGEMENTS

This work was funded by the NOMAD Center of Excellence (European Union's Horizon 2020 research and innovation program, grant agreement Nº 951786), the ERC Advanced Grant TEC1p (European Research Council, grant agreement Nº 740233), and the project FAIRmat (FAIR Data Infrastructure for Condensed-Matter Physics and the Chemical Physics of Solids, German Research Foundation, project Nº 460197019). T.P. would like to thank the Alexander von Humboldt (AvH) Foundation for their support through the AvH Postdoctoral Fellowship Program. This research used resources of the Argonne Leadership Computing Facility, which is a DOE Office of Science User Facility supported under Contract DE-AC02-06CH11357 and the Max Planck Computing and Data Facility.

V. DATA AVAILABILITY

All raw electronic structure data can be found on the NOMAD archive (`https://dx.doi.org/10.17172/NOMAD/2022.04.27-1`).

VI. ONLINE METHODS

A. SISSO

We use SISSO to discover new analytical expressions for $\kappa_L\,(300\mathrm{K})$ [52]. SISSO finds low-dimensional, analytic expressions for a target property, P, by first generating an exhaustive set of candidate features, $\hat{\Phi}$, for a given set of primary features, $\hat{\Phi}_0$, and operators $\hat{\mathcal{H}}_m$, and then performing an ℓ_0-regularization over a subset of those features to find the n-dimensional subset of features, whose linear combination results in the most descriptive model. $\hat{\Phi}$ is recursively built in rungs, $\hat{\mathcal{F}}_r$, from $\hat{\Phi}_0$ and $\hat{\mathcal{H}}_m$, by applying all elements, $\hat{\mathrm{h}}^m$, of $\hat{\mathcal{H}}^m$ on all elements $\hat{\mathrm{f}}_i$ and $\hat{\mathrm{f}}_j$ of $\hat{\mathcal{F}}_{r-1}$

$$\hat{\mathcal{F}}_r \equiv \hat{\mathrm{h}}^m\left[\hat{\mathrm{f}}_i, \hat{\mathrm{f}}_j\right], \forall\, \hat{\mathrm{h}}^m \in \hat{\mathcal{H}}^m \text{ and } \forall\, \hat{\mathrm{f}}_i, \hat{\mathrm{f}}_j \in \hat{\mathcal{F}}_{r-1}.$$

$\hat{\Phi}_r$ is then the union of $\hat{\Phi}_{r-1}$ and $\hat{\mathcal{F}}_r$. Once $\hat{\Phi}$ is generated, the $n_{\rm SIS}$ features most correlated to P are stored in $\hat{\mathcal{S}}_1$, and the best one-dimensional models are trivially extracted from the top elements of $\hat{\mathcal{S}}_1$. Then the $n_{\rm SIS}$ features most correlated to any of the residuals, $\mathbf{\Delta}_1^i$, of the $n_{\rm res}$ best one-dimensional descriptors are stored in $\hat{\mathcal{S}}_2$. We define this projection as

$$s = \max\left(s_0, s_1, ..., s_i, ..., s_{\rm n_{res}}\right) \tag{3}$$

$$s_i = R^2\left(\hat{\phi}, \mathbf{\Delta}_1^i\right), \tag{4}$$

where $\hat{\phi} \in \hat{\Phi}$, and R^2 is the Pearson correlation function. We call this approach the multiple residual approach, which we first introduced by the authors [53]. From here, the best two dimensional models are found by performing an ℓ_0-regularized optimization over $\hat{\mathcal{S}}_1 \cup \hat{\mathcal{S}}_2$ [54]. This process is iteratively repeated until the best n-dimensional descriptor is found [52].

For this application $\hat{\mathcal{H}}_m$ contains: $A + B$, $A - B$, $A * B$, $\frac{A}{B}$, $|A - B|$, $|A|$, $(A)^{-1}$, $(A)^2$, $(A)^3$, $\sqrt{A}$, $\sqrt[3]{A}$, $\exp(A)$, $\exp(-1.0 * A)$, and $\ln(A)$. Additionally to ensure the units of the primary features do not affect the final results, we additionally include the following operators: $(A + \beta)^{-1}$, $(A + \beta)^2$, $(A + \beta)^3$, $\sqrt{\alpha A + \beta}$, $\sqrt[3]{A + \beta}$, $\exp(\alpha A)$, $\exp(-1.0 * \alpha A)$, and $\ln(\alpha A + \beta)$, where α and β are scaling and bias constants used to adjust the input data on the fly. We find the optimal α and β terms using non-linear optimization for each of these operators [21, 55]. To ensure that the parameterization does not result in mathematically invalid equations for new data points outside of the training set, the domain of each candidate feature is derived from the domain of the primary features, and the upper and lower bounds for the features are set appropriately. The domains of the primary features are set to be physically relevant for the systems we are studying and are listed in Table II. Hereafter, we call the use of these operators parametric SISSO. For more information please refer to Supplementary Note 1.

All hyperparameters were set following the cross-validation procedures described in Section VI D.

B. KRR

To generate the kernel-ridge regression models we used the utilities provided by scikit-learn [56], using a radial basis function kernel with optimized regularization term and kernel length scale. The hyperparameters were selected using with a 141 by 141 point logarithmic grid search with possible parameters ranging from 10^{-7} to 10^0. Before performing the analysis each input feature, $\mathbf{x}_{\rm i}$ is standardized

$$\mathbf{x}_{\rm i}^{\rm Stand} = \frac{\mathbf{x}_{\rm i} - \mu_{\rm i}}{\sigma_{\rm i}} \tag{5}$$

where $\mathbf{x}_{\rm i}^{\rm stand}$ is the standardized input feature, $\mu_{\rm i}$ is the mean of the input feature for the training data, and $\sigma_{\rm i}$ is the standard deviation of the input feature for the training data.

C. Creating the Dataset

In this study we focus on only room-temperature data for $\kappa_{\rm L}$, since values for other temperatures are even scarcer. However, we note that an explicit temperature dependence can be straightforwardly included using multi-task SISSO [53, 57], and it is at least partially included via, the anharmonicity factor, $\sigma^{\rm A}$ [8] (see below for more details). For κ_L (300K), we have compiled a list of seventy-five materials from the literature, whose thermal conductivity has been experimentally measured [17, 25–42]. This list was curated from an initial set of over 100 materials, from which we removed all materials that are either thermodynamically unstable or are electrical conductors. This list of materials covers a diverse set of fourteen different binary and ternary crystal structure prototypes [49, 50, 58].

With respect to the primary features, $\hat{\Phi}_0$, compound specific properties are provided for each material. All primary features can be roughly categorized in two classes: Structural parameters that describe the equilibrium structure and dynamical parameters that characterize the nuclear motion. For the latter case, both harmonic properties and anharmonic have been taken into account. As shown in Supplementary Note 3, additional features, such as the parameters entering the Slack model, i.e., γ, $\Theta_{\rm a}$, and $V_{\rm a}$, can be included. However, these features not benefit the model and when included only $V_{\rm a}$, and not γ or $\Theta_{\rm a}$ are selected. For a complete list of all primary features, and their definitions refer to Table II.

The structural parameters relate to either the mass of the atoms (μ, $m_{\rm min}$, $m_{\rm max}$, $m_{\rm avg}$), the lattice parameters of the primitive cell ($V_{\rm m}$, $L_{\rm min}$, $L_{\rm max}$, $L_{\rm avg}$), the density of the materials (ρ), or the number of atoms in the primitive cell ($n_{\rm at}$). For all systems a generalization of the reduced mass, μ, is used so it can be extended to non-binary systems,

$$\mu = \left(\sum_i^{n_{\rm emp}} \frac{1}{m_i}\right)^{-1}, \tag{6}$$

where $n_{\rm emp}$ is the number of atoms in the empirical formula and m_i is the mass of atom, i. Similarly, the molar volume, $V_{\rm m}$, is calculated by

$$V_{\rm m} = \frac{V_{\rm prim}}{Z}, \tag{7}$$

where $V_{\rm prim}$ is the volume of the primitive cell and $Z = \frac{n_{\rm at}}{n_{\rm emp}}$. Finally, ρ is calculated by dividing the total mass of the empirical cell by $V_{\rm m}$

$$\rho = \sum_i^{n_{\rm emp}} \frac{m_i}{V_{\rm m}}. \tag{8}$$

TABLE II. List of the primary features used in this calculation

Name	Symbol	Unit	Domain
Anharmonicity Score (aiMD) [8]	σ^{A}	—	[0.075, 1.0]
Anharmonicity Score (one-shot [8])	$\sigma^{\mathrm{A}}_{\mathrm{OS}}$	—	[0.075, 1.0]
Maximum Phonon Frequency at the Γ-point	$\omega_{\Gamma,\mathrm{max}}$	THz	[0.1, 200]
High-Temperature Limit of the Debye Temperature	$\Theta_{\mathrm{D},\infty}$	K	[10, 1 000]
Average Phonon Temperature	Θ_{P}	K	[10, 10 000]
Heat Capacity	C_{V}	J mol^{-1} K^{-1}	[10, 5 000]
Speed of sound	v_{s}	m s^{-1}	[500, 10 000]
Density	ρ	Da Å^{-3}	[0.25, 10]
Molar Volume	V_{m}	Å^3	[2.5, 1 000]
Minimum Lattice Parameter	L_{min}	Å	[1, 100]
Maximum Lattice Parameter	L_{max}	Å	[1, 100]
Mean Lattice Parameter	L_{avg}	Å	[1, 100]
Reduced Mass	μ	Da	[0.2, 300]
Minimum Atomic Mass	m_{min}	Da	[1, 300]
Maximum Atomic Mass	m_{max}	Da	[1, 300]
Mean Atomic Mass	m_{avg}	Da	[1, 300]
Number of Atoms	n_{at}	$\mathbb{Z}$	[1, 1 000]

All of the harmonic properties used in these calculations are calculated from a converged harmonic model generated using phonopy [59]. For each material, the phonon density of states of successively larger supercells are compared using a Tanimoto similarity measure

$$S = \frac{g_{\mathrm{p,L}}(\omega) \cdot g_{\mathrm{p,S}}(\omega)}{\|g_{\mathrm{p,L}}(\omega)\|^2 + \|g_{\mathrm{p,S}}(\omega)\|^2 - g_{\mathrm{p,L}}(\omega) \cdot g_{\mathrm{p,S}}(\omega)}, \quad (9)$$

where S is the similarity score, $g_{\mathrm{p,L}}(\omega)$ is the phonon density of states of the larger supercell, $g_{\mathrm{p,S}}(\omega)$ is the phonon density of states of the smaller supercell, $A(\omega) \cdot B(\omega) = \int_0^\infty A(\omega) B(\omega) d\omega$, and $\|A(\omega)\|^2 = \int_0^\infty A^2(\omega) d\omega$. If $S > 0.80$, then the harmonic model is considered converged. From here C_{V} is calculated from phonopy as a weighted sum over the mode dependent heat capacities. Both approximations to the Debye temperatures are calculated from the moments of the phonon density of states

$$\langle \varepsilon^n \rangle = \frac{\int d\varepsilon\, g_p(\varepsilon)\, \varepsilon^n}{\int d\varepsilon g_p(\varepsilon)} \quad (10)$$

$$\Theta_{\mathrm{P}} = \frac{1}{k_B} \langle \varepsilon \rangle \quad (11)$$

$$\Theta_{\mathrm{D},\infty} = \frac{1}{k_B} \sqrt{\frac{5}{3} \langle \varepsilon^2 \rangle}, \quad (12)$$

where $g_p(\varepsilon)$ is the phonon density of states at energy ε [60]. Finally v_{s} is approximated from the Debye frequency, ω_{D}, by [20]

$$v_{\mathrm{s}} = \left(\frac{V_{\mathrm{a}}}{6\pi^2} \right)^{1/3} \omega_{\mathrm{D}}, \quad (13)$$

where ω_{D} is approximated as

$$\omega_{\mathrm{D}} = \sqrt[3]{\frac{9 n_{\mathrm{at}}}{a}} \quad (14)$$

and a is found by fitting $g_p(\omega)$ in the range $\left[0, \frac{\omega_{\Gamma,\mathrm{max}}}{8}\right]$ to

$$g_{p,D}(\omega) = a\omega^2. \quad (15)$$

To measure the anharmonicity of the materials we use σ^{A} as defined in [8]

$$\sigma^{\mathrm{A}}(T) = \sqrt{\frac{\sum\limits_{I,\alpha} \left\langle \left(F_{I,\alpha} - F^{\mathrm{ha}}_{I,\alpha} \right)^2 \right\rangle_{(T)}}{\sum_{I,\alpha} \left\langle F^2_{I,\alpha} \right\rangle_{(T)}}}, \quad (16)$$

in which $\langle \cdot \rangle_{(T)}$ denotes the thermodynamic average at a temperature T, $F_{I,\alpha}$ is the α component of the force calculated from density functional theory (DFT) acting on atom I, and $F^{\mathrm{ha}}_{I,\alpha}$ is the same force approximated by the harmonic model [8]. First we calculate $\sigma^{\mathrm{A}}_{\mathrm{OS}}$, which uses an approximation to the thermodynamic ensemble average using the one-shot method purposed by Zacharias and Giustino [61]. In the one-shot approach the atomic positions are offset from their equilibrium positions by a vector $\mathbf{\Delta R}$,

$$\Delta R^\alpha_I = \frac{1}{\sqrt{M_I}} \sum_s \zeta_s \langle A_s \rangle e^\alpha_{sI}, \quad (17)$$

where I is the atom number, α is the component, $\mathbf{e}_s$ are the harmonic eigenvectors, $\langle A_s \rangle = \sqrt{2 k_{\mathrm{B}} T}/\omega_s$ is the

mean mode amplitude in the classical limit [62], and $\zeta_s = (-1)^{s-1}$ [61]. These displacements correspond to the turning-points of the oscillation estimated from the harmonic force constants, and is a good approximation to σ^{A} in the harmonic limit. Because of this, if $\sigma^{\mathrm{A}}_{\mathrm{OS}} < 0.2$ we accept that value as the true σ^{A}. Otherwise we calculate σ^{A} using ab initio molecular dynamics (aiMD) in the canonical ensemble at 300 K for 10 ps, using the Langevin thermostat. When performing the high-throughput screening the threshold for when to use aiMD is increased to 0.4 because that is the point that $\sigma^{\mathrm{A}}_{\mathrm{OS}}$ become qualitatively unreliable [8].

All electronic structure calculations are done using FHI-aims [63]. All geometries are optimized with symmetry-preserving, parametric constraints until all forces are converged to a numerical precision better than 10^{-3} eV/Å [64]. The constraints are generated using the AFlow XtalFinder Tool [58]. All calculations use the PBEsol functional to calculate the exchange-correlation energy and an SCF convergence criteria of 10^{-6} eV/Å and 5×10^{-4} eV/Å for the density and forces, respectively. Relativistic effects are included in terms of the scalar atomic ZORA approach and all other settings are taken to be the default values in FHI-aims. For all calculations we use the *light* basis sets and numerical settings in FHI-aims. These settings were shown to ensure a convergence in lattice constants of ±0.1 Å and a relative accuracy in phonon frequencies of 3% [8].

D. Error Evaluation

To estimate the prediction error for the SISSO and KRR models we perform a nested cross-validation, where the data are initially separated into different training and test sets using a ten-fold split. Two hyperparameters (maximum dimension, parameterization depth) are then optimized using a five-fold cross validation on each of the training sets, and the overall performance of the model is evaluated on the corresponding test set. The size of the SIS subspace, number of residuals, and rung were all set to 2 000, 10, and 3, respectively, because they did not have a large impact on the final results. We then repeat procedure three times and average over each iteration to get a reliable estimate of prediction error for each sample [65].

E. Calculating the inputs to the Slack model

The individual components for the Slack model were the same as the ones used for the SISSO and KRR models, with the exception of γ, V_{a} and Θ_{a}. For Θ_{a}, we first calculate the Debye temperature, Θ_{D}

$$\Theta_{\mathrm{D}} = \frac{\hbar\omega_{\mathrm{D}}}{k_{\mathrm{B}}} \tag{18}$$

where ω_{D} is the same Debye frequency used for calculating v_{s} (see Section VI C), k_{B} is the Boltzmann constant, and $\hbar$ is Planck's constant. From here we calculate Θ_{a} using

$$\Theta_{\mathrm{a}} = \frac{\Theta_{\mathrm{D}}}{\sqrt[3]{n_{\mathrm{at}}}}. \tag{19}$$

We use the phonopy definition of Θ_{D} instead of $\Theta_{\mathrm{D},\infty}$ because it is better aligned to the original definition of Θ_{a}. However, it is not used in the SISSO training because the initial fitting procedure to find ω_{D} does not produce a unique value for Θ_{D} and it is already partially included via v_{s}. To calculate the thermodynamic Grüneisen parameter we use the utilities provided by phonopy [59]. The atomic volume was calculated by taking the volume of the primitive cell and dividing it by the total number of atoms.

F. Calculating the Sobol Indexes

Formally, the Sobol indices are defined as

$$S_i = \frac{\mathrm{Var}_{\hat{x}_i}\left(E_{\widetilde{\mathcal{X}}_i}\left(\log\left(\kappa_L\left(300\mathrm{K}\right)\right)|\hat{x}_i\right)\right)}{\mathrm{Var}\left(\log\left(\kappa_L\left(300\mathrm{K}\right)\right)\right)} \tag{20}$$

$$S_i^T = 1 - \frac{\mathrm{Var}_{\widetilde{\mathcal{X}}_i}\left(E_{\hat{x}_i}\left(\log\left(\kappa_L\left(300\mathrm{K}\right)\right)|\widetilde{\mathcal{X}}_i\right)\right)}{\mathrm{Var}\left(\log\left(\kappa_L\left(300\mathrm{K}\right)\right)\right)} \tag{21}$$

where $\hat{x}_i \in \hat{\mathcal{X}}$ is one of the inputs to the model, $\mathrm{Var}_a\left(B\right)$ is the variance of B with respect to a, $E_a\left(B\right)$ is the mean of B after sampling over a, and $\widetilde{\mathcal{X}}_i$ is the set of all variables excluding $\hat{x}_i$.

Classically it is assumed that all elements of $\hat{\mathcal{X}}$ are independent of each other. As a result of this, the variance of $\log\left(\kappa^{\mathrm{SISSO}}\left(300\mathrm{K}\right)\right)$ and the required expectation values would be calculated from sampling over an n_v-dimensional hypercube covering the full input range, ignoring the correlation between the inputs variables. In order to properly model the correlative effects between elements of $\hat{\mathcal{X}}$, Kucherenko et al. modify this sampling approach [43, 45]. The first step of the updated algorithm is to fit the input data to a set of marginal univariate distributions coupled together via a copula [43, 45]. The algorithm then samples over an n_v-dimensional unit-hypercube and transforms these samples into the correct variable space using a transform defined by the fitted distributions and copulas (see Supplementary Note 2 for more details). It was later demonstrated that when using the approach proposed by Kucherenko and coworkers to calculate the Sobol indices, S_i includes effects from the dependence of $\hat{x}_i$ on those in $\widetilde{\mathcal{X}}_i$, while S_i^T is independent of these effects [66].

G. Calculating the Thermal Conductivity

To calculate κ_{L}, we use the *ab initio* Green Kubo (aiGK) method [10, 67]. The aiGK method calculates the $\alpha\beta$ component of the thermal conductivity tensor, $\kappa^{\alpha\beta}$, of a material for a given volume V, pressure p, and temperature T with

$$\kappa^{\alpha\beta}\left(T,p\right)=\frac{V}{k_{B}T^{2}}\lim_{\tau\rightarrow\infty}\int_{0}^{\tau}\langle G\left[\boldsymbol{J}\right]^{\alpha\beta}\left(\tau'\right)\rangle_{(T,p)}d\tau' \quad (22)$$

where k_B is Boltzmann's constant, $\langle\cdot\rangle_{(T,p)}$ denotes an ensemble average, $\boldsymbol{J}\left(t\right)$ is the heat flux, and $G\left[\boldsymbol{J}\right]$ is the time-(auto)correlation functions

$$G\left[\boldsymbol{J}\right]^{\alpha\beta}=\lim_{t_{0}\rightarrow\infty}\frac{1}{t_{0}}\int_{0}^{t_{0}-\tau}J^{\alpha}\left(t\right)J^{\beta}\left(t+\tau\right)dt. \quad (23)$$

The heat flux of each material is calculated from aiMD trajectories using the following definition

$$\boldsymbol{J}\left(t\right)=\sum_{i}\boldsymbol{\sigma}_{I}\dot{\boldsymbol{R}}_{y}I, \quad (24)$$

where $\boldsymbol{R}_I$ is the position of the i^{th}-atom and $\boldsymbol{\sigma}_I$ is the contribution of the i^{th} atom to the stress tensor, $\boldsymbol{\sigma}=\sum_I\boldsymbol{\sigma}_I$ [10]. From here κ_{L} is calculated as

$$\kappa_{\mathrm{L}}=\frac{1}{3}\mathrm{Tr}\left[\boldsymbol{\kappa}\right] \quad (25)$$

All calculations were done using both FHI-vibes [68] and FHI-aims with the same settings as the previous calculations [8] (see Section VI C for more details). The molecular dynamics calculations were done using a 5 fs time step in the NVE ensemble, with the initial structures taken from a 10 ps NVT trajectory. Three MD calculations were done for each material and the κ_{L} was taken to be the average of all three runs.

[1] V. Stanev, K. Choudhary, A. G. Kusne, J. Paglione, and I. Takeuchi, Commun. Mater. **2**, 105 (2021).
[2] S. A. Miller, P. Gorai, B. R. Ortiz, A. Goyal, D. Gao, S. A. Barnett, T. O. Mason, G. J. Snyder, Q. Lv, V. Stevanović, and E. S. Toberer, Chem. Mater. **29**, 2494 (2017).
[3] C. P. Gomes, B. Selman, and J. M. Gregoire, MRS Bull. **44**, 538 (2019).
[4] Q. Zhang, E. Uchaker, S. L. Candelaria, and G. Cao, Chem. Soc. Rev. **42**, 3127 (2013).
[5] B. Christian Enger, R. Lødeng, and A. Holmen, Appl. Catal. A Gen. **346**, 1 (2008).
[6] W. Wu, G. Zhang, X. Ke, X. Yang, Z. Wang, and C. Liu, Energy Convers. Manag. **101**, 278 (2015).
[7] T. M. Pollock, Nat. Mater. **15**, 809 (2016).
[8] F. Knoop, T. A. R. Purcell, M. Scheffler, and C. Carbogno, Phys. Rev. Mater. **4**, 083809 (2020), arXiv:2006.14672.
[9] D. A. Broido, M. Malorny, G. Birner, N. Mingo, and D. A. Stewart, Appl. Phys. Lett. **91**, 231922 (2007).
[10] C. Carbogno, R. Ramprasad, and M. Scheffler, Phys. Rev. Lett. **118**, 175901 (2017), arXiv:1608.06917.
[11] J. Carrete, W. Li, N. Mingo, S. Wang, and S. Curtarolo, Phys. Rev. X **4**, 11019 (2014).
[12] A. Seko, A. Togo, H. Hayashi, K. Tsuda, L. Chaput, and I. Tanaka, Phys. Rev. Lett. **115**, 205901 (2015).
[13] Y. Xia, Appl. Phys. Lett. **113**, 073901 (2018).
[14] T. Zhu, R. He, S. Gong, T. Xie, P. Gorai, K. Nielsch, and J. C. Grossman, Energy Environ. Sci. **14**, 3559 (2021).
[15] "Springer Materials," http://materials.springer.com.
[16] Y. Zhang and C. Ling, npj Comput. Mater. **4**, 25 (2018).
[17] L. Chen, H. Tran, R. Batra, C. Kim, and R. Ramprasad, Comput. Mater. Sci. **170**, 109155 (2019), arXiv:1906.06378.
[18] G. A. Slack, in *Solid State Phys. - Adv. Res. Appl.*, Vol. 34 (Academic Press, 1979) pp. 1–71.
[19] J. Yan, P. Gorai, B. Ortiz, S. Miller, S. A. Barnett, T. Mason, V. Stevanović, and E. S. Toberer, Energy Environ. Sci. **8**, 983 (2015).
[20] E. S. Toberer, A. Zevalkink, and G. J. Snyder, J. Mater. Chem. **21**, 15843 (2011).
[21] T. A. R. Purcell, M. Scheffler, C. Carbogno, and L. M. Ghiringhelli, J. Open Source Softw. **7**, 3960 (2022).
[22] G. R. Schleder, C. M. Acosta, and A. Fazzio, ACS Appl. Mater. Interfaces **12**, 20149 (2020).
[23] Z.-K. Han, D. Sarker, R. Ouyang, A. Mazheika, Y. Gao, and S. V. Levchenko, Nat. Commun. **12**, 1833 (2021).
[24] G. Pilania, C. N. Iverson, T. Lookman, and B. L. Marrone, J. Chem. Inf. Model. **59**, 5013 (2019).
[25] D. T. Morelli and G. A. Slack, in *High Therm. Conduct. Mater.* (Springer, New York, NY, New York, 2006) pp. 37–68.
[26] G. A. Slack, Phys. Rev. **126**, 427 (1962).
[27] J. Martin, J. Phys. Chem. Solids **33**, 1139 (1972).
[28] T. Takahashi and T. Kikuchi, J. Nucl. Mater. **91**, 93 (1980).
[29] P. Turkes, C. Pluntke, and R. Helbig, J. Phys. C Solid State Phys. **13**, 4941 (1980).
[30] D. Gerlich and P. Andersson, J. Phys. C Solid State Phys. **15**, 5211 (1982).
[31] R. K. Williams, R. S. Graves, and D. L. McElroy, J. Am. Ceram. Soc. **67**, C (2006).
[32] M. Valeri-Gil and C. Rincón, Mater. Lett. **17**, 59 (1993).
[33] D. T. Morelli, T. Caillat, J.-P. Fleurial, A. Borshchevsky, J. Vandersande, B. Chen, and C. Uher, Phys. Rev. B **51**, 9622 (1995).
[34] H. Hohl, A. P. Ramirez, C. Goldmann, G. Ernst, B. Wölfing, and E. Bucher, J. Phys. Condens. Matter **11**, 1697 (1999).
[35] D. P. Young, P. Khalifah, R. J. Cava, and A. P. Ramirez, J. Appl. Phys. **87**, 317 (2000).
[36] J.-G. Li, T. Ikegami, and T. Mori, J. Mater. Res. **18**, 1816 (2003).

[37] Y. Kawaharada, K. Kurosaki, H. Muta, M. Uno, and S. Yamanaka, J. Alloys Compd. **384**, 308 (2004).

[38] E. G. Víllora, K. Shimamura, Y. Yoshikawa, T. Ujiie, and K. Aoki, Appl. Phys. Lett. **92**, 202120 (2008).

[39] C. Toher, J. J. Plata, O. Levy, M. de Jong, M. Asta, M. B. Nardelli, and S. Curtarolo, Phys. Rev. B **90**, 174107 (2014), arXiv:1407.7789.

[40] Y. Lu, T. Nozue, N. Feng, K. Sagara, H. Yoshida, and Y. Jin, J. Alloys Compd. **650**, 558 (2015).

[41] W. Huang, B. Zhao, S. Zhu, Z. He, B. Chen, Z. Zhen, Y. Pu, and W. Liu, J. Cryst. Growth **443**, 8 (2016).

[42] S. Pantian, R. Sakdanuphab, and A. Sakulkalavek, Curr. Appl. Phys. **17**, 1264 (2017).

[43] S. Kucherenko, S. Tarantola, and P. Annoni, Comput. Phys. Commun. **183**, 937 (2012).

[44] S. Marelli and B. Sudret, "UQLab: A Framework for Uncertainty Quantification in Matlab," in *Vulnerability, Uncertainty, Risk* (American Society of Civil Engineers, Reston, VA, 2014) pp. 2554–2563.

[45] P. Wiederkehr, *Global Sensitivity Analysis with Dependent Inputs*, Ph.D. thesis, ETH Zurich (2018).

[46] S. Razavi, A. Jakeman, A. Saltelli, C. Prieur, B. Iooss, E. Borgonovo, E. Plischke, S. Lo Piano, T. Iwanaga, W. Becker, S. Tarantola, J. H. Guillaume, J. Jakeman, H. Gupta, N. Melillo, G. Rabitti, V. Chabridon, Q. Duan, X. Sun, S. Smith, R. Sheikholeslami, N. Hosseini, M. Asadzadeh, A. Puy, S. Kucherenko, and H. R. Maier, Environ. Model. Softw. **137**, 104954 (2021).

[47] R. E. Peierls, *Quantum theory of solids* (Oxford University Press, 1955) pp. 47–89.

[48] A. Jain, S. P. Ong, G. Hautier, W. Chen, W. D. Richards, S. Dacek, S. Cholia, D. Gunter, D. Skinner, G. Ceder, and K. A. Persson, APL Mater. **1** (2013), 10.1063/1.4812323.

[49] M. J. Mehl, D. Hicks, C. Toher, O. Levy, R. M. Hanson, G. Hart, and S. Curtarolo, Comput. Mater. Sci. **136**, S1 (2017).

[50] D. Hicks, M. J. Mehl, E. Gossett, C. Toher, O. Levy, R. M. Hanson, G. Hart, and S. Curtarolo, Comput. Mater. Sci. **161**, S1 (2019).

[51] C. Duan, F. Liu, A. Nandy, and H. J. Kulik, J. Phys. Chem. Lett. **12**, 4628 (2021).

[52] R. Ouyang, S. Curtarolo, E. Ahmetcik, M. Scheffler, and L. M. Ghiringhelli, Phys. Rev. Mater. **2**, 83802 (2018).

[53] L. Foppa, L. M. Ghiringhelli, F. Girgsdies, M. Hashagen, P. Kube, M. Hävecker, S. J. Carey, A. Tarasov, P. Kraus, F. Rosowski, R. Schlögl, A. Trunschke, and M. Scheffler, MRS Bull. **46**, 1016 (2021), arXiv:2102.08269.

[54] L. M. Ghiringhelli, J. Vybiral, E. Ahmetcik, R. Ouyang, S. V. Levchenko, C. Draxl, and M. Scheffler, New J. Phys. **19**, 023017 (2017), arXiv:1612.04285.

[55] S. G. Johnson, "The NLopt nonlinear-optimization package," http://github.com/stevengj/nlopt.

[56] F. Pedregosa, G. Varoquaux, A. Gramfort, V. Michel, B. Thirion, O. Grisel, M. Blondel, P. Prettenhofer, R. Weiss, V. Dubourg, J. Vanderplas, A. Passos, D. Cournapeau, M. Brucher, M. Perrot, and E. Duchesnay, J. Mach. Learn. Res. **12**, 2825 (2011).

[57] R. Ouyang, E. Ahmetcik, C. Carbogno, M. Scheffler, and L. M. Ghiringhelli, J. Phys. Mater. **2**, 24002 (2019).

[58] D. Hicks, C. Toher, D. C. Ford, F. Rose, C. D. Santo, O. Levy, M. J. Mehl, and S. Curtarolo, npj Comput. Mater. **7**, 30 (2021), arXiv:2010.04222.

[59] A. Togo and I. Tanaka, Scr. Mater. **108**, 1 (2015).

[60] R. Pässler, J. Appl. Phys. **101**, 093513 (2007).

[61] M. Zacharias and F. Giustino, Phys. Rev. B **94**, 75125 (2016).

[62] M. Dove, *Introduction to lattice dynamics* (Cambridge University Press, 1993).

[63] V. Blum, R. Gehrke, F. Hanke, P. Havu, V. Havu, X. Ren, K. Reuter, and M. Scheffler, Comput. Phys. Commun. **180**, 2175 (2009).

[64] M.-O. Lenz, T. A. R. Purcell, D. Hicks, S. Curtarolo, M. Scheffler, and C. Carbogno, npj Comput. Mater. **5**, 123 (2019).

[65] D. Krstajic, L. J. Buturovic, D. E. Leahy, and S. Thomas, J. Cheminform. **6**, 10 (2014).

[66] T. A. Mara, S. Tarantola, and P. Annoni, Environ. Model. Softw. **72**, 173 (2015).

[67] N. K. Ravichandran and D. Broido, Phys. Rev. B **98**, 085205 (2018).

[68] F. Knoop, T. A. R. Purcell, M. Scheffler, and C. Carbogno, J. Open Source Softw. **5**, 2671 (2020).